


Article

Imaging of the Upper Mantle Beneath Southeast Asia: Constrained by Teleseismic P-Wave Tomography

Huiyan Shi ¹ , Tonglin Li ¹, Rongzhe Zhang ^{1,*}, Gongcheng Zhang ² and Hetian Yang ¹

¹ College of Geo-Exploration Science and Technology, Jilin University, Changchun 130026, China; hys19@mails.jlu.edu.cn (H.S.); litl@jlu.edu.cn (T.L.); htyang19@mails.jlu.edu.cn (H.Y.)

² CNOOC Research Institute, Beijing 100028, China; zhanggch@cnooc.com

* Correspondence: zhangrz@jlu.edu.cn

Received: 31 July 2020; Accepted: 10 September 2020; Published: 13 September 2020



Abstract: It is of great significance to construct a three-dimensional underground velocity model for the study of geodynamics and tectonic evolution. Southeast Asia has attracted much attention due to its complex structural features. In this paper, we collected relative travel time residuals data for 394 stations distributed in Southeast Asia from 2006 to 2019, and 14,011 seismic events were obtained. Then, teleseismic tomography was applied by using relative travel time residuals data to invert the velocity where the fast marching method (FMM) and subspace method were used for every iteration. A novel 3D P-wave velocity model beneath Southeast Asia down to 720 km was obtained using this approach. The tomographic results suggest that the southeastern Tibetan Plateau, the Philippines, Sumatra, and Java, and the deep part of Borneo exhibit high velocity anomalies, while low velocity anomalies were found in the deep part of the South China Sea (SCS) basin and in the shallow part of Borneo and areas near the subduction zone. High velocity anomalies can be correlated to subduction plates and stable land masses, while low velocity anomalies can be correlated to island arcs and upwelling of mantle material caused by subduction plates. We found a southward subducting high velocity body in the Nansha Trough, which was presumed to be a remnant of the subduction of the Dangerous Grounds into Borneo. It is further inferred that the Nansha Trough and the Dangerous Grounds belong to the same tectonic unit. According to the tomographic images, a high velocity body is located in the deep underground of Indochina–Natuna Island–Borneo–Palawan, depth range from 240 km to 660 km. The location of the high velocity body is consistent with the distribution range of the ophiolite belt, so we speculate that the high velocity body is the remnant of the Proto-South China Sea (PSCS) and Paleo-Tethys. This paper conjectures that the PSCS was the southern branch of Paleo-Tethys and the gateway between Paleo-Tethys and the Paleo-Pacific Ocean. Due to the squeeze of the Australian plate, PSCS closed from west to east in a scissor style, and was eventually extinct under Borneo.

Keywords: 3-D velocity model; teleseismic tomography; Fast Marching Method; subspace method; Southeast Asia; Proto-South China Sea

1. Introduction

The Proto-South China Sea (PSCS) refers to the ocean that was once located in the southeastern part of China in the area where the South China Sea (SCS) now stands [1–4]. In a narrower sense, it was believed that the PSCS was a subduction of the SCS region at the Eurasian continental margin from Izonaki to Eurasia, and that the formation of the PSCS was due to the rollback of the Izonaki subduction plate to form a spreading environment and the pulling apart of the post-arc basin [5–7]. Numerous scholars have carried out extensive research in the PSCS remnant zone. A set of ophiolite remained from the PSCS has been identified using geological data, which is distributed in an arc along

Natuna Island–Kalimantan Island–Palawan Island [8]; others have applied the tomography method to the region, and it was inferred that the PSCS remained in the deep mantle of the southern Philippines region [9], and it has also been suggested that the remnant of the PSCS presents in the mantle of the SCS basin [10,11]. Taylor and Hayes suggested that the PSCS existed in the Middle Triassic to Late Cretaceous Tertiary based on magnetic anomalies, paleo-magnetic, and paleontological evidence [3]. While Liu defined the PSCS as an eastern extension of the Middle Tethys based on regional geological and geophysical data and inferred a Late Permian date for its emergence [1]; Wu inferred the earliest existence of the PSCS in the Triassic period based on Mesozoic stratigraphic and fossil characteristics in the southern SCS [12]; Zhou et al. inferred that the PSCS has existed since the Late Jurassic–Early Cretaceous based on deep-sea radiolarians in the serpentine suite of the Natuna–Kalimantan–Palawan distribution, and that it may be a back-arc sea formed by subduction of the Pacific plate [13]; Metcalfe argued that the PSCS was formed when the Cretaceous East Asian continental margins pulled apart by studying the tectonic shelf of the Epiphytic Sundaland [14]; Lu studied the influence of Tethys and Paleo-Pacific on the PSCS through regional geological, paleontological, gravity, and magnetic anomalies [15]; numerous scholars have also determined the existence of the PSCS from 70 Ma to 10 Ma through plate reconstruction methods [7,16].

Considering the location of the PSCS, which is the junction of the Paleo-Pacific Ocean and Tethys, the Tethys tectonic domain has been extensively studied by previous researchers [17–21], and some scholars had also commented on the Paleo-Pacific of tectonic evolution for reconstruction [22–26]. However, due to the limitations of data and research methods as well as the complexity of the tectonic evolution of the Paleo-Pacific and Tethys tectonic domains, the relationship between the PSCS and Tethys tectonic domains and the Paleo-Pacific has not been clarified clearly.

Seismic tomography has the advantage of a large detection depth and has been widely applied to study the deep structure and tectonic evolution [27]. Extensive excellent work has been carried out by previous researchers in SE Asia [28–32]. Based on previous studies, this paper used the latest seismic data that can be collected in Southeast Asia to study its velocity structure. Relative travel time residuals data from 2006 to 2019 were collected for 394 stations in the study area. The teleseismic tomography method was used to invert the P-wave velocity structure of the study area. Finally, a three-dimensional P-wave velocity model was obtained, which was beneath SE Asia. Combined with the results of previous studies, the distribution range of the PSCS, the location of subduction extinction, and its relationship with the Paleo-Pacific and Tethys tectonic domain can be summarized as follows. Figure 1 shows a sketch of the tectonic and topography in Southeast Asia.

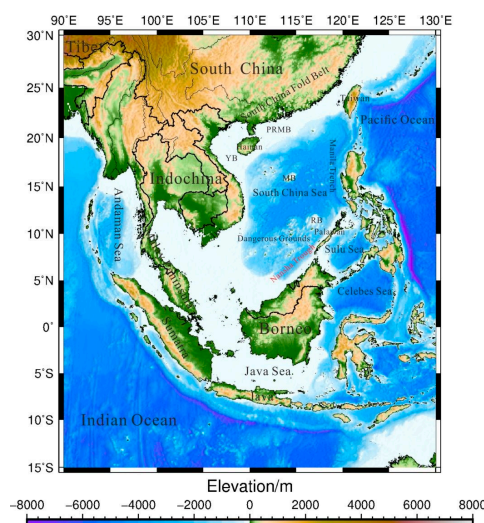


Figure 1. Sketch of the tectonic and topographic map of Southeast Asia. The meanings of the abbreviations in the figure are: PRMB, Pearl River Mouth Basin; YB, Yinggehai Basin; MB, Macclesfield Bank; RB, Reed Bank.

2. Data

The seismic data used in this paper were primarily derived from the Incorporated Research Institutions for Seismology (IRIS) [33] and International Seismic Center (ISC) [34]. The research range is (15° S– 30° N, 90° E– 130° E). To satisfy the requirement of the subsequent inversion calculation, data were collected according to the following criteria: (1) The seismic events used for the inversion have magnitudes greater than 5.0; (2) The distances from the station to hypocenter were between 30° and 90° , minimizing the impact of the complex structure of the lower mantle and core mantle boundary [35]; 3. Seismic events used for inversion must be recorded by at least five stations simultaneously. The final collection was 14,011 seismic events recorded from 394 seismic stations in the study area, and 180,225 useful P-wave relative travel time residuals were obtained for inversion. Compared to previous work, this study added data from one new station at the Dangerous Grounds. Therefore, the results of this study are more reliable than those of the previous work. The distribution of stations in the study area and the distribution of seismic sources used for inversion calculation are shown in Figure 2a,b, respectively.

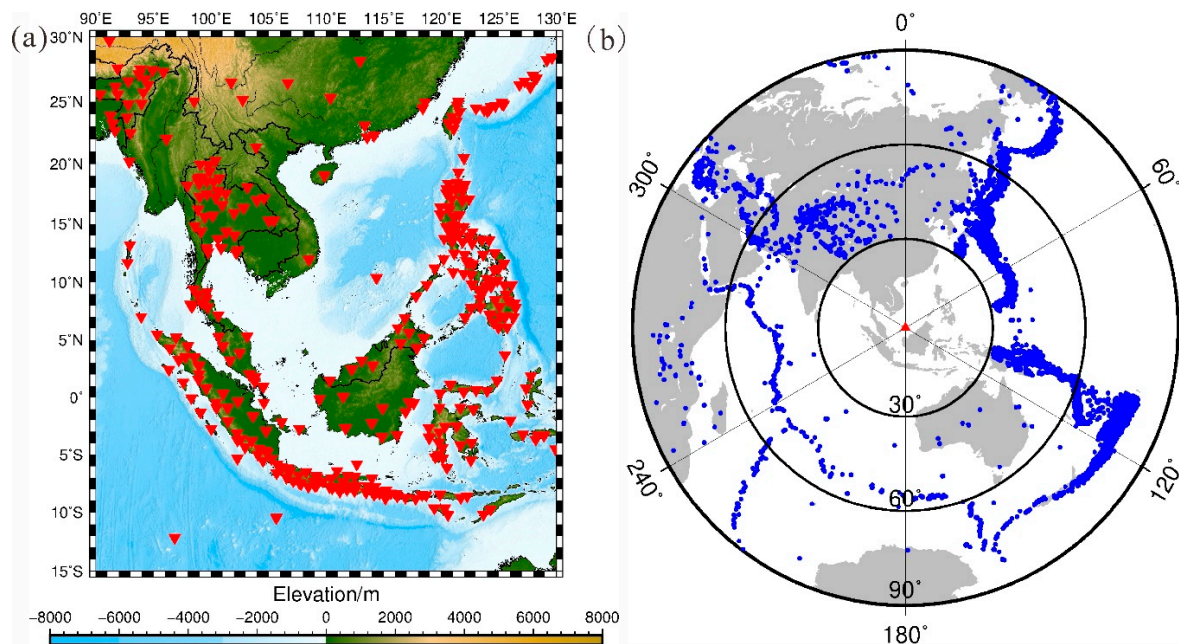


Figure 2. (a) Distribution of 394 seismic stations in the South China Sea (SCS) and surrounding areas; (b) Distribution of seismic sources for teleseismic tomography imaging of 14,011 teleseismic events.

To obtain the relative travel time residual data for inversion calculations, it is necessary to pick up the P-wave first arrival time of the collected raw seismic waveform data. Manually picking each waveform data will be a very time-consuming work. Seismologists have proposed a number of proven methods for picking up the P-wave first arrival time based on the principle of waveform correlation [36–38]. A graphical interface program for picking up relative travel time residuals was developed by Zhang [38], which combined two methods of picking up the relative travel time residuals together. This program greatly improved the efficiency of picking up relative travel time residuals. The work of picking up relative travel time residuals in this paper benefited from this program.

The process of picking up relative travel time residuals based on the above method is shown in Figure 3 [39]. First, the appropriate recoding of teleseismic events were downloaded and filtered according to the study acquisition requirements. Second, the raw data was band-pass filtered before the pickup work. The frequency range of 0.01–1 Hz was chosen to avoid filtering out the relatively high-frequency information of the teleseismic events. The first arrival time of the P-wave can be better preserved. You can also adjust the range based on the sampling rate of the data. The next step is to

select the theoretical travel time provided by the ak135 model to align the waveform data with each other, and perform the inter-correlation process on its theoretical travel time. We used the adaptive stacking (astack) method [40] and multi-channel cross correlation (MCC) method [36] to superimpose the waveform data, and then compared the difference between the residuals obtained by the two picking methods. Waveforms with a P-wave first arrival error greater than 0.2 s and a shape obviously different will be deleted. Repeat the above steps until all the picked results are within the error range. This process of picking up relative travel time residuals guarantees accuracy as much as possible [41]. Figure 4 shows the waveform pickup window for a magnitude 6.1 earthquake on 22 June 2008.

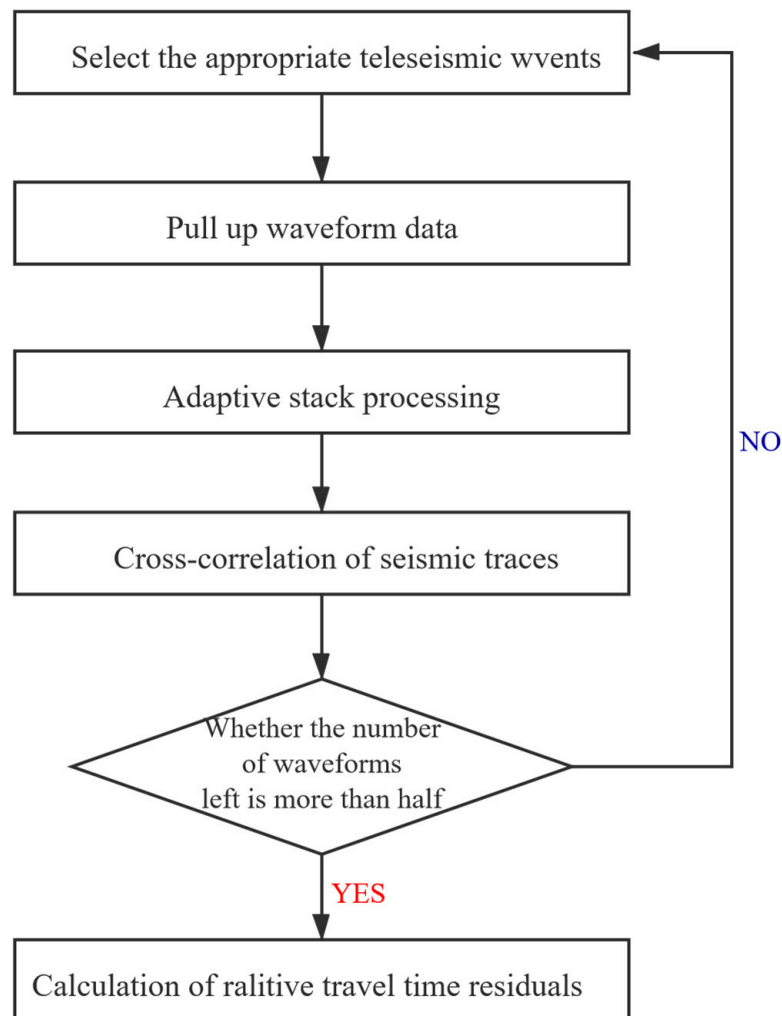


Figure 3. Flowchart of picking up relative travel time residuals from raw seismic waveform data (modified from Jia, Z. [39]).

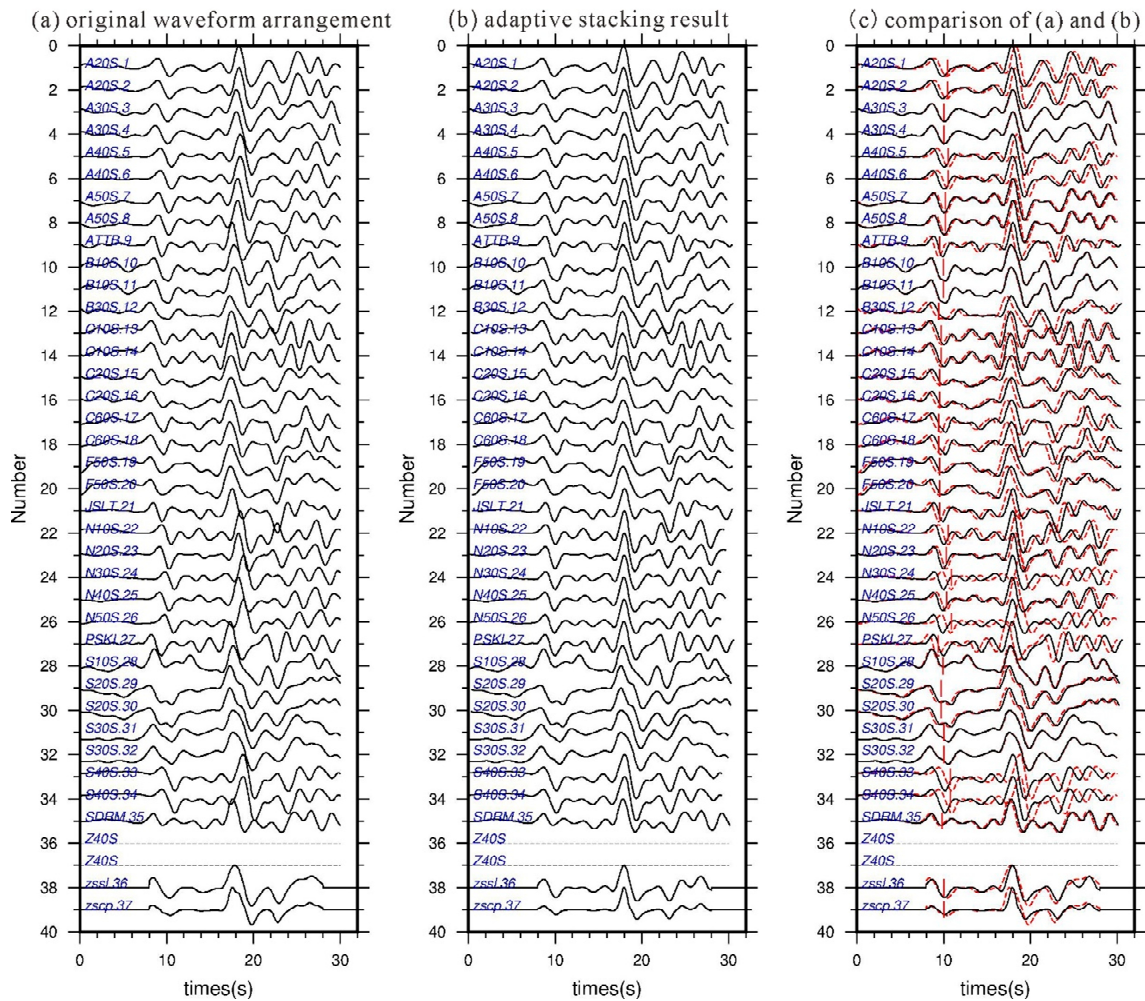


Figure 4. Waveform pickup window for a magnitude 6.1 earthquake on 22 June 2008. (a) This panel shows the original waveform. (b) This panel shows the adaptive stacking result. (c) This panel shows the comparison of (a) and (b). The combination of numbers and letters represent station names. The red vertical lines in panel (c) mark the position of the P-wave first arrival time by ak135.

3. Methodology

The principle of the teleseismic tomography imaging method is shown in Figure 5. First, we need to dissect the subsurface structure beneath the receiver array in the study area into a gridded model. This model will be placed into a globally symmetric reference model [42–44]. Figure 5 illustrates the principle of teleseismic tomography. As shown in Figure 5, a local gridded model is located beneath the receiver array, which contains 3D variations in velocity. Regions outside the local gridded model are assumed to be spherically symmetric. The advantage of this pattern is that the travel time from the seismic source to the local gridded model boundary can be predicted quickly. The travel time inside the local gridded model is calculated by ray-tracing techniques for laterally heterogeneous media [45]. The premise of the above principle is that the lateral variations outside the local gridded model will not significantly affect the relative travel time residuals. In other words, all relative travel time residuals at the stations are then assumed to be only caused by the local anomalies.

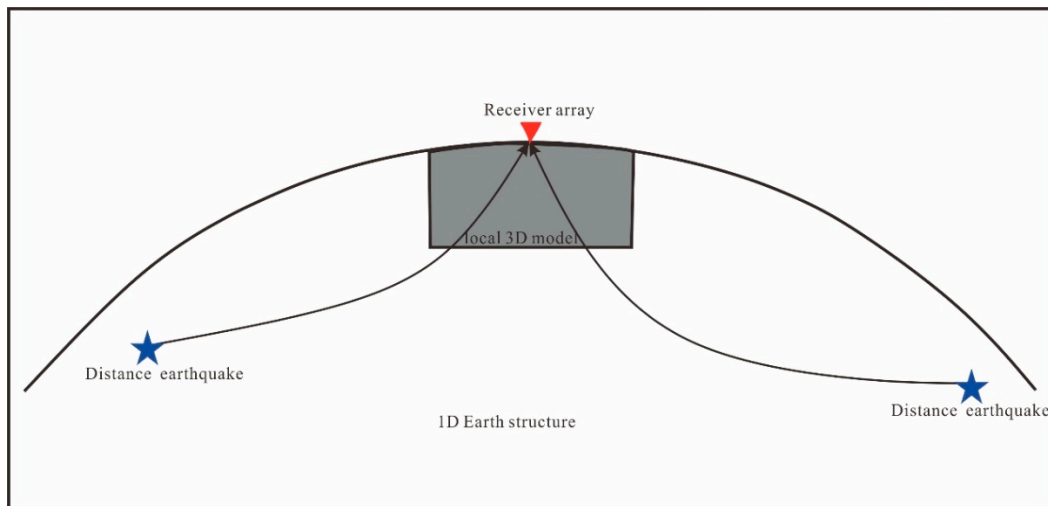


Figure 5. The principle of the teleseismic tomography. The red triangular denotes the receiver array. The blue stars denote the distance earthquake [45].

The teleseismic tomography process can be divided into model parameterization, forward step, and inversion step. The following description of the inversion scheme is described according to these steps.

3.1. Model Parameterization

Model parameterization refers to the process of using a series of constant or changing nodes or blocks to characterize velocity variations. The following form is used to formulate the slowness field within a 3D spherically symmetric grid of nodes [46]:

$$s(r, \theta, \phi) = \sum_{i,j,k=1}^4 S_{ijk} C_i(R) C_j(\Theta) C_k(\Phi) \quad (1)$$

where S_{ijk} represents the slowness at the nodes of the $4 \times 4 \times 4$ grid surrounding the point (r, θ, ϕ) . $C_i(R)$, $C_j(\Theta)$, and $C_k(\Phi)$ are known as the cardinal splines, and R , Θ , and Φ are local coordinates of r , θ , and ϕ [46].

Conventional cubic spline interpolation has been widely applied in travel time tomography [47–50]. Spline passing through node values is essential for traditional cubic spline interpolation. The form of interpolation function cubic B-splines used in this paper was similar to Equation (1). This was locally supported and did not necessarily pass through the node values.

3.2. Forward Step

The next step of teleseismic tomography scheme is the forward step. The aim of the forward step in the inverse problem is calculating the theoretical travel times of waves.

In travel time inversion, the conventional method of calculating source-receiver travel time was the ray-tracing technique. More recently, the eikonal equation has been widely applied in travel time inversion [47]. The following eikonal equation governed the path of seismic waves in the local gridded model:

$$|\nabla_x T| = s(x) \quad (2)$$

In Equation (2), T represents travel time and $s(x)$ represents slowness as a function of position x . The core of the FMM method is to solve Equation (2) with an upwind entropy that satisfies

finite differences. In this paper, we used the following form, which has been employed by other authors [48,49]:

$$\left[\begin{array}{c} \max(D_a^{-r}T, -D_b^{+r}T, 0)^2 \\ \max(D_c^{-\theta}T, -D_d^{+\theta}T, 0)^2 \\ \max(D_e^{-\phi}T, -D_f^{+\phi}T, 0)^2 \end{array} \right]_{i,j,k}^{\frac{1}{2}} = S_{i,j,k} \quad (3)$$

In Equation (3), (i, j, k) denote grid increment variables in (r, θ, ϕ) . The integer variable a, b, c, d, e, f is used to determine the order of accuracy of the upwind finite-difference operator used in each of the six portions. If (r, θ, ϕ) represents a spherical coordinate system, the first two gradient operators in each of the three directions can be described by the following form:

$$\begin{aligned} D_1^{-r}T_{i,j,k} &= \frac{T_{i,j,k} - T_{i-1,j,k}}{\delta r} \\ D_2^{-r}T_{i,j,k} &= \frac{3T_{i,j,k} - 4T_{i-1,j,k} + T_{i-2,j,k}}{2\delta r} \\ D_1^{-\theta}T_{i,j,k} &= \frac{T_{i,j,k} - T_{i,j-1,k}}{r\delta\theta} \\ D_2^{-\theta}T_{i,j,k} &= \frac{3T_{i,j,k} - 4T_{i,j-1,k} + T_{i,j-2,k}}{2r\delta\theta} \\ D_1^{-\phi}T_{i,j,k} &= \frac{T_{i,j,k} - T_{i,j,k-1}}{r\cos\theta\delta\phi} \\ D_2^{-\phi}T_{i,j,k} &= \frac{3T_{i,j,k} - 4T_{i,j,k-1} + T_{i,j,k-2}}{2r\cos\theta\delta\phi} \end{aligned} \quad (4)$$

The operator used in Equation (4) depends on the availability of upwind travel times and the max order allowed. By default, we used a mixed order form which used empirical D_2 operators but reverted to D_1 if $T_{i-2,j,k}$, $T_{i,j-2,k}$, or $T_{i,j,k-2}$ was unavailable [47]. Equation (3) describes the finite difference form for calculating the travel time associated with a specified grid node. However, the order of updating grid nodes have not been specified. To satisfy causality, the values of T should change from small to large. To satisfy the above rule, FMM systematically constructs the travel time in a downwind manner based on known values in the upwind direction. This is called the narrowband approach. Figure 6 illustrates the principle of the multi-stage FMM approach. A detailed explanation of this method can be found in [49].

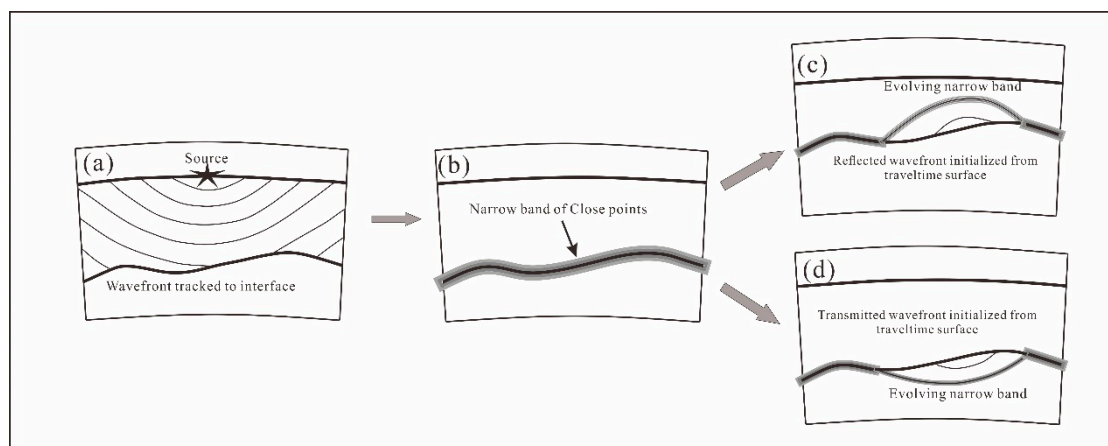


Figure 6. Illustration of the multi-stage Fast Marching Method (FMM) approach principle. The incident wave front is tracked to all points on the wave front, before reinitializing FMM in the incident or adjacent layer. (a) Incident wavefront generated from a point source; (b) Narrow band determined by a serial interface nodes; (c) reflected wavefront tracked; (d) refracted wavefront tracked [51].

3.3. Inversion Step

The essence of seismic tomography inversion is to solve the optimization problem. The subspace method can be minimized simultaneously along the search direction, and across a subspace of the

model space, which is illustrated in Figure 7. The following form is the most common objection function used in inversion:

$$S(m) = (g(m) - d_{obs})^T C_d^{-1} (g(m) - d_{obs}) + \varepsilon (m - m_0)^T C_m^{-1} (m - m_0) \tag{5}$$

There is a basic assumption before using gradient methods that when $S(m)$ is smooth enough, the following form can be obtained:

$$S(m + \delta m) \approx S(m) + \hat{\gamma} \delta m + \frac{1}{2} \delta m^T \hat{H} \delta m \tag{6}$$

In the above form, δm indicates a disturbance to the current model, and $\hat{\gamma} = \frac{\partial S}{\partial m}$ indicates the gradient vector; $\hat{H} = \frac{\partial^2 S}{\partial m^2}$ indicates the Hessian matrix. Combining the above partial differences gives the following forms [50]:

$$\hat{\gamma} = G^T C_d^{-1} [g(m) - d_{obs}] + \varepsilon C_m^{-1} (m - m_0) \tag{7}$$

$$\hat{H} = G^T C_d^{-1} G + \nabla_m G^T C_d^{-1} [g(m) - d_{obs}] + \varepsilon C_m^{-1} \tag{8}$$

In Equations (7) and (8) $G = \frac{\partial g}{\partial m}$ denotes the *Fréchet* matrix of partial derivatives. For the case of constant slowness blocks $G = [l_{ij}]$, l_{ij} indicates the ray segment length of the i^{th} ray in the j^{th} block.

The general theory for the normal subspace inversion method has been explained by some scholars [51–53]. The subspace method limits the minimization of the quadratic approximation of $S(m)$ to an n -dimensional subspace of model space, so that the disturbance δm occurs in the space spanned by a set of n M -dimensional basis vectors $\{a^j\}$:

$$\delta m = \sum_{j=1}^n \mu_j a^j = A \mu \tag{9}$$

In Equation (9), μ_j is the component defining the length of the corresponding vector a^j that minimizes the quadratic form of $S(m)$ in the space. Equation (6) takes the following form:

$$S(m + \delta m) = S(m) + \sum_{j=1}^n \mu_j \hat{\gamma}^T a^j + \frac{1}{2} \sum_{j=1}^n \sum_{k=1}^n \mu_j \mu_k [a^k]^T \hat{H} [a^j] \tag{10}$$

and searches for the minimum values of S considering μ :

$$\frac{\partial S(m)}{\partial \mu_q} = \hat{\gamma}^T a^q + \sum_{k=1}^n \mu_k [a^k]^T \hat{H} [a^j] = 0 \tag{11}$$

When $q = 1, \dots, n$, the following form can be obtained from Equation (9):

$$\mu = -[A^T \hat{H} A]^{-1} A^T \hat{\gamma} \tag{12}$$

where $\delta m = A \mu$, and $\hat{H} = G^T C_d^{-1} G + \varepsilon C_m^{-1}$, and the following form obtained:

$$\delta m = -A [A^T (G^T C_d^{-1} G + \varepsilon C_m^{-1}) A]^{-1} A^T \hat{\gamma} \tag{13}$$

The quantities A , $\hat{\gamma}$, and G are re-evaluated between successive iterations. The construction of the basis vector $\{a^j\}$ for the subspace approach is typically done with the steepest upward vector and rate of change in the model space [51–54].

The subspace method has been applied to invert the velocity, interface structure, and hypocenter location using local earthquake and artificial source travel times [53–56]. The inversion scheme has been successfully applied in northern Tasmania and the Murray Basin [57,58]

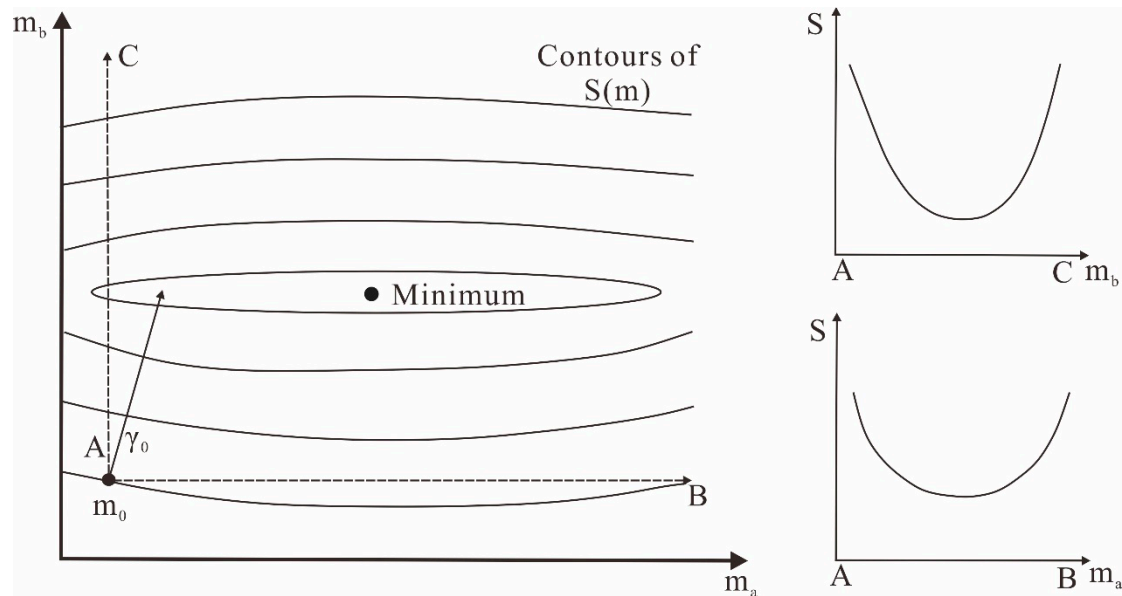


Figure 7. The principle of the subspace method [59]. The left panel shows a contour of $S(m)$, which is a function of two parameters of different physical dimensions. The right panel suggests that $S(m)$ is more sensitive to m_b than m_a .

4. Crust Correction

When using teleseismic tomography to study the velocity structure of the upper mantle, the complex crustal structure may affect the tomographic results of the upper mantle [60–64]. To ensure the accuracy of the upper mantle velocity imaging results, crust correction is needed to eliminate the influence of the crust. Many scholars have carried out research in this area [65–67]. In this paper, the method proposed by Jiang [67] is used for crustal correction of teleseismic imaging. The idea of this method is to obtain the relative travel time residuals inside the crust before the inversion calculation, and then process the relative travel time residuals of the entire ray.

The main steps of crustal correction are:

(1) Select the appropriate 1-D crustal model and 3-D crustal model. The 1-D crustal model in this article was obtained from AK135 [68], and the 3-D crustal model was the CRUST1.0 [69];

(2) Calculate the travel time of the ray in the 1-D model and the 3-D model of the crust respectively, and then calculate the relative travel time residual in the crust, the calculation formula, takes the following form:

$$\delta T_{crust} = T_{3D} - T_{1D} = \left(\sum_l \frac{h_l}{\cos \theta_l \times V_l} \right)_{3D} - \left(\sum_k \frac{h_k}{\cos \theta_k \times V_k} \right)_{1D} \quad (14)$$

where δT_{crust} denotes the relative travel time residuals in the crust. T_{3D} and T_{1D} represent the travel time in the crust, respectively. h_l and h_k represent the thickness of each layer in 1-D and 3-D models, respectively. θ_l and θ_k represent the incident angle of the ray at each interface in 1-D and 3-D models, respectively.

(3) Subtract the relative travel time residual in the crust from the relative travel time residual of the ray, and use it as the inversion data of teleseismic tomography.

$$t = (T_{obs} - T_{cal}) - \delta T_{crust} \quad (15)$$

where t indicates the relative travel time residuals of rays. T_{obs} and T_{cal} represent the observed travel time and theoretical travel time, respectively.

Figure 8 shows the distribution of the average relative residuals at each station before and after crust correction and the change of average relative travel time residuals. From Figure 8a,b, the difference between the average of each station before and after crustal correction to travel time residuals is very small, ranging from -2.4 s to 2.4 s after crustal correction. Figure 8c reveals that the variation of the average travel time residual of each station ranged from -0.09 s to 0.09 s.

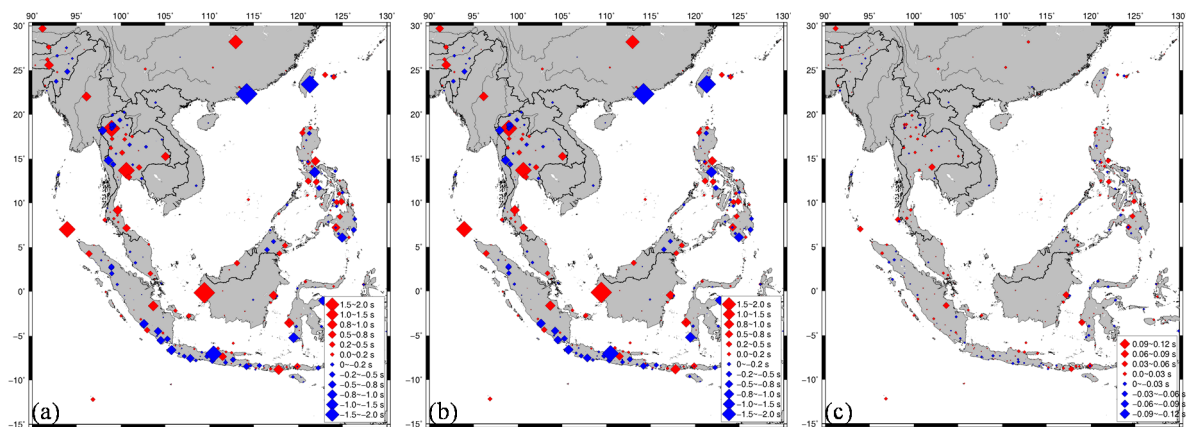


Figure 8. (a) Distribution of average relative travel time residuals at each station before crust correction. (b) Distribution of average relative travel time residuals at each station after crust correction. (c) Distribution of the change of average relative travel time residuals at each station after crust correction.

5. Resolution Test

Before displaying the tomographic imaging, we used the checkerboard test method to check the stability and resolution of the model [70]. The specific steps of the checkerboard test are as follows: (1) Establish an initial model 1 and a model 2 based on the initial model 1 with positive and negative disturbance velocity anomalies added; (2) Use model 2 as the initial model to calculate the theoretical relative travel time residuals of each ray of the observation system consisting of stations and events in the study area; (3) Use model 1 as the initial model and use the theoretical travel time obtained in step (2) to calculate residuals used in the inversion step, and model 3 was obtained through inversion calculations. Comparing the velocity anomaly images of model 2 and model 3, the smallest anomaly scale that could be recovered in model 3 was the resolution of the model [41].

During the checkerboard test in this study, a plus or minus 0.3 km/s perturbation was added to the theoretical model. In the vertical direction, the resolutions of the 40 km, 60 km, and 90 km grids were tested, and the results suggested that when the vertical grid was 90 km, the model had the best recovery effect. In the horizontal direction, the checkerboard test results revealed that the most optimal grid space was $1.65^\circ \times 1.65^\circ$.

Figure 9 shows the checkerboard test results in the horizontal, latitude, and longitude directions. Figure 9a(I) is a horizontal slice of the input model at 100 km, and Figure 9a(II), Figure 9a(IV), and Figure 9a(VI) are the slices of the output model at 100 km, 400 km, and 600 km, respectively. According to the results of the checkerboard test, when the depth was 100 km, the recovery effect of the output model was good in most areas of the study area. Only the southwestern area of the study area and the central area of the SCS basin showed poor recovery effects. The main reason is that these two areas are both marine areas so there are fewer stations and sparse rays. Figure 9a(III), Figure 9a(V), and Figure 9a(VII) show the distribution of ray paths at 100 km, 400 km, and 600 km, respectively. When the depth increased, the recovery effect of the South China Sea basin gradually improved. Figure 9b show the results of the checkerboard test in the latitude direction. Figure 9b(I) is a slice of the input checkerboard model along the 0° direction, and Figure 9b(II) and Figure 9b(III) are

slices of the output model along the 0° and 12° N, respectively. It can be seen that the recovery effect of the slice in the 0° direction was very good. The recovery effect of the velocity anomalies in the area of 110°E – 115°E on the slice along 12°N was not very ideal, while the recovery effect of the velocity anomalies in other areas was very good. Figure 9c shows the results of the checkerboard test in the longitude direction. Figure 9c(I) shows the slice of the input model along 104°E . Figure 9c(II) and Figure 9c(III) are the slices of the output model along 104°E and 114°E , respectively. It can be seen that the velocity anomalies of the slice along 104°E recovered well. The overall recovery effect of the slice along 112°E was very good. The shallow recovery effect of 10° – 15° was slightly worse, which was caused by the scarcity of stations in the ocean area. In general, the effect of the checkerboard test is relatively satisfactory. The velocity model obtained in this study had a large scale, so it was mainly used to study the large-scale structural evolution. According to the results of the checkerboard test, the model used in this study had a denser ray distribution in the upper mantle and mantle transition zone, so the inversion results in this depth range are more reliable.

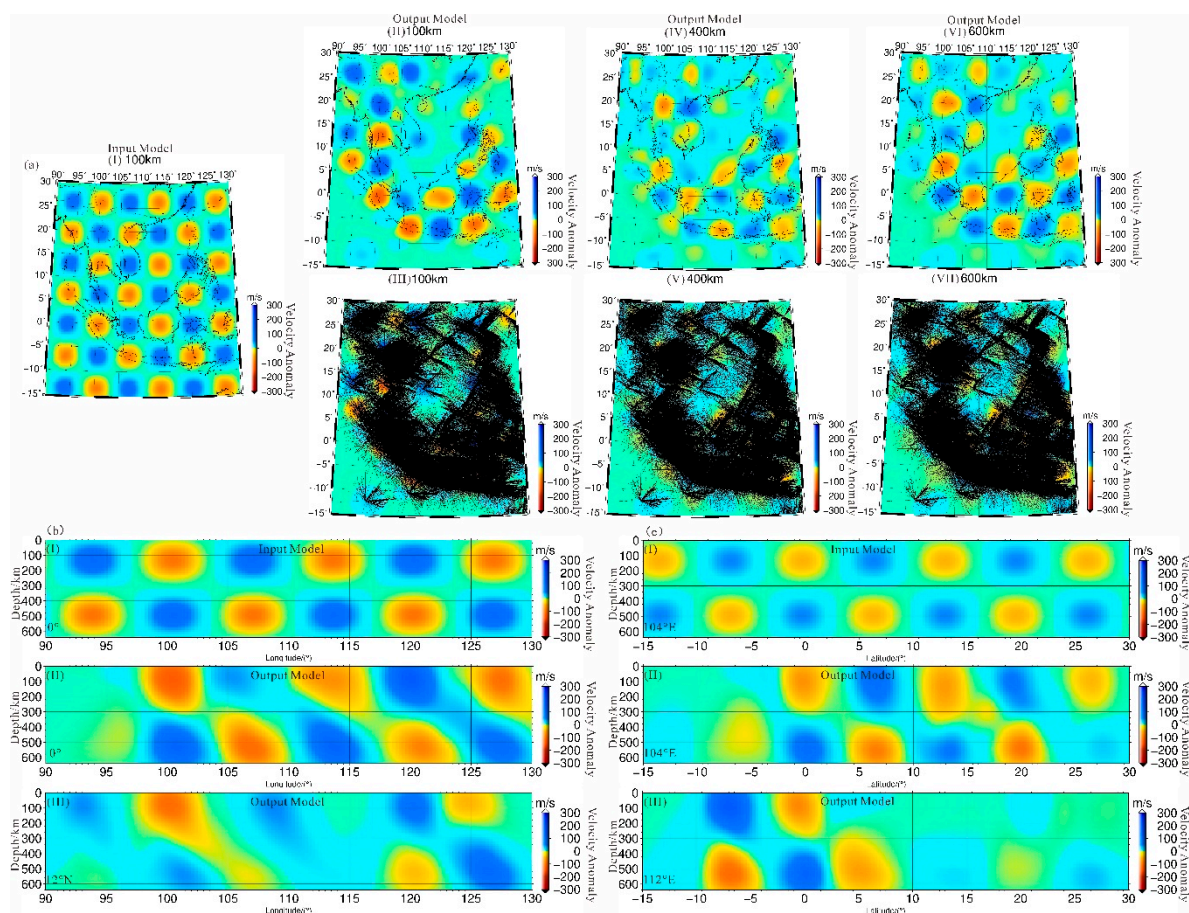


Figure 9. Results of checkerboard test in three directions and ray paths. (a) Horizontal slices; (b) Vertical slices along east–west direction; (c) Vertical slices along the north–south direction.

In order to apply the above-mentioned tomographic method to obtain the 3D velocity model beneath SE Asia, the local model beneath the receiver array was first parameterized. The structure under 394 stations in the study area was divided into 27,225 nodes. During the inversion, the vertical grid space was 90 km, and the grid space in the longitude and latitude directions was 1.65° (~ 160 km). The above parameters were selected based on the checkerboard test results. The depth of the local gridded model in the vertical direction was down to 720 km, the range in the longitude direction was 40° , and the range in the latitude direction was 45° . The reference velocity model was given by ak135. After six iterations of inversion, an inversion result was obtained. The observed relative

travel time residuals and the theoretical relative travel time residuals were highly matched. Figure 10 shows the distribution of the observed relative travel time residuals and the post-inversion relative travel time residuals, respectively. Observed data and the inversion results were normally distributed, indicating that the initial model evolved along the direction of the fitting anomaly after the inversion calculation. This further verifies the reliability of the inversion results, indicating that the inversion results are reasonable.

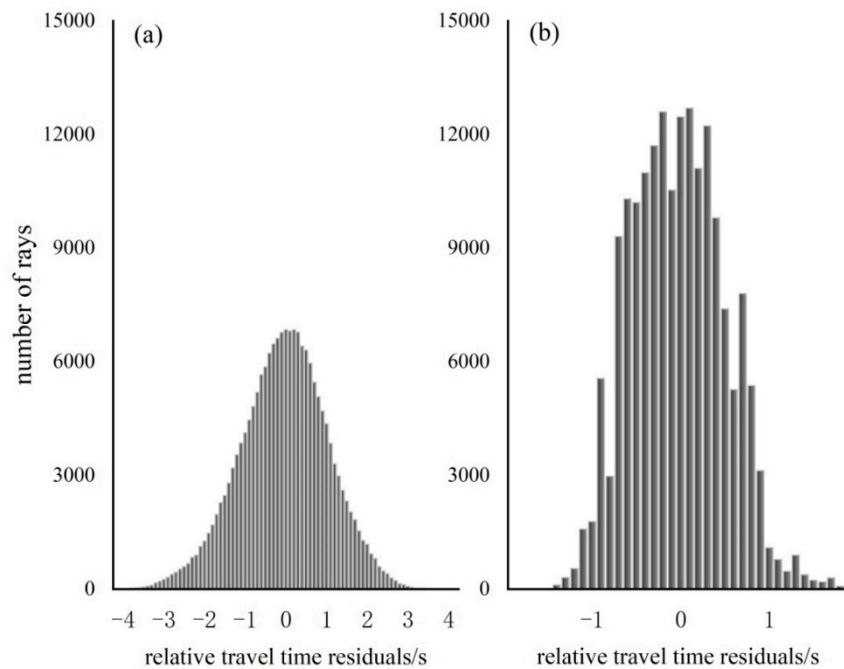


Figure 10. (a) Histogram of the relative travel time residuals distribution before inversion. (b) Histogram of relative travel time residuals distribution after inversion.

6. Results

Map views of the P-wave tomography at nine depths are shown in Figure 11. Overall, the velocity anomalies at different depths had good correspondence with the associated tectonic units. When the depth was smaller than 200 km, it can be seen that the southeastern Tibet Plateau, the South China Plate, the Philippines, the Indochina Peninsula and Java showed obvious high-velocity anomalies. The Dangerous Grounds and the western region of Borneo also exhibited high-velocity anomalies, while low-velocity anomalies were mainly located in areas such as the Malay Peninsula, Sumatra, and Borneo. As the depth increased, the anomaly distribution characteristics of the study area changed. When the depth was between 250 km and 630 km, the Tibet Plateau and the South China Plate and the Philippines still exhibited the characteristics of high-velocity anomalies. The area from the Andaman Sea along Sumatra to Java changed from low-velocity to high-velocity, just like a high-velocity anomaly covered with a low-velocity anomaly. This phenomenon was also found in the previous study [33]. It is worth noting that the high-velocity anomaly area of the Indochina Peninsula had become larger and showed a trend of spreading from north to south. The area outside the western part of Borneo also changed from a low-velocity anomaly in the shallow to a high-velocity anomaly. The high-velocity anomalies in these two areas tended to be integrated. The overall route is shown in Figure 11, from the depth of 200 km–630 km with red arrows. This area was the focus of this paper. In addition, the velocity anomalies in the SCS basin also changed from high-velocity anomalies to low-velocity anomalies. The characteristics of velocity anomalies below 700 km were like those at 630 km. High-velocity anomalies mainly occur in the subduction zone, shallow ocean basin, and continental area, while low-velocity anomalies occur in the deep ocean basin and associate locations with high-velocity anomalies. Previous studies have suggested that the low-velocity area

may reflect the upwelling of mantle material, and was mainly caused by plate subduction and lower mantle collapse [71,72].

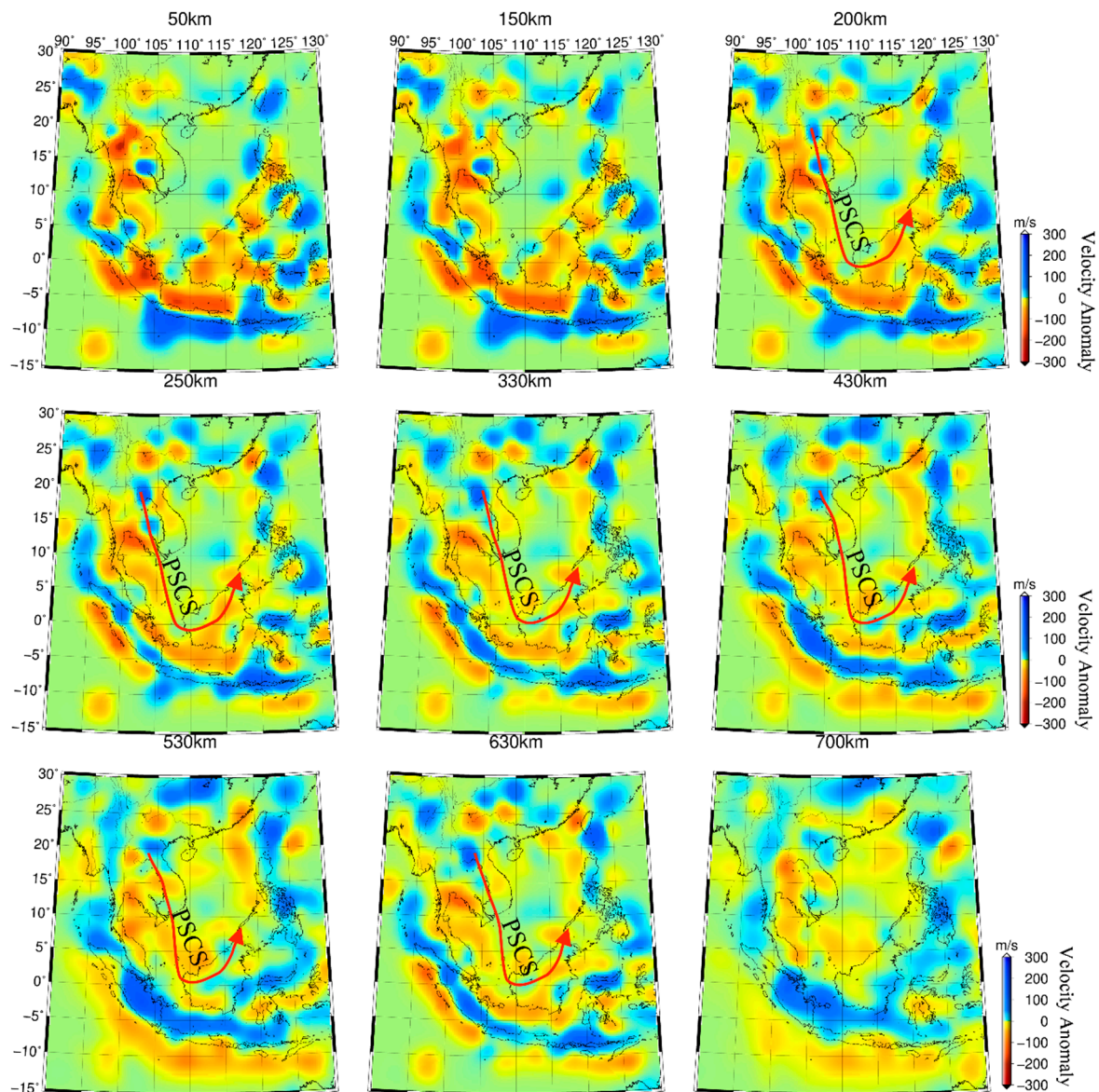


Figure 11. Tomographic slices at nine depths in the horizontal direction. Red color and blue color represent the low and high velocity anomalies, respectively. On the right side of the figure is the scale of the velocity anomaly.

Figures 12 and 13 show the slices along the east–west and north–south directions, respectively. As can be seen in the east–west slices (Figure 12), the shallow part of the Andaman Sea and the SCS basin exhibited high-velocity anomalies. The deep areas of the Philippines, Sumatra, and Java exhibited high-velocity anomalies. The low-velocity anomalies in the shallow areas covered the high-velocity anomalies in the deep area. As can be seen in the north–south slices (Figure 13), the Indochina, the South China Plate, and the shallower part of the SCS basin exhibited high-velocity anomalies, while in the subduction zone such as Sumatra and Java, it is characterized by shallow low-velocity anomalies covering deep high-velocity anomalies. The slices results are more supportive of the possibility that the low-velocity region near the subduction zone was due to material upwelling caused by plate subduction into the mantle [71,72].

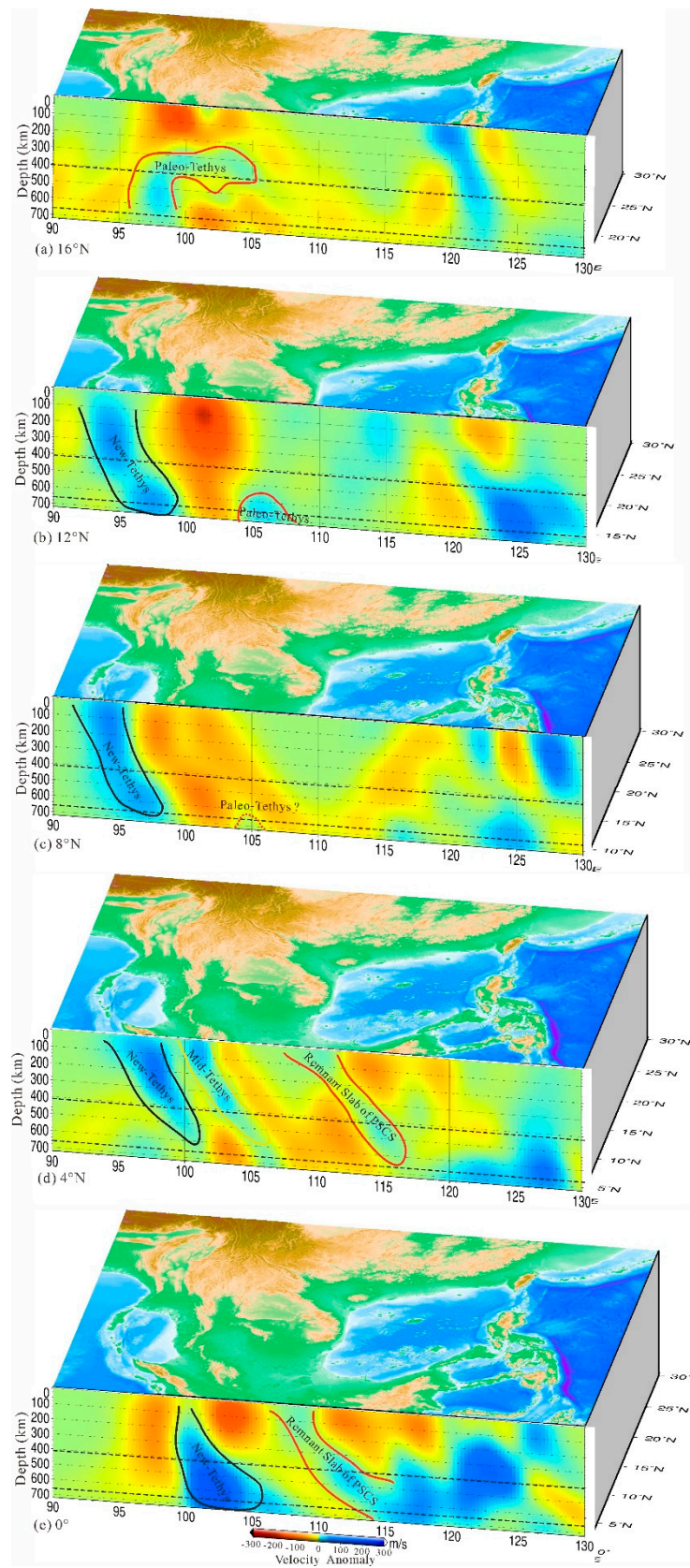


Figure 12. Five vertical slices of the P-wave velocity tomography along the latitude direction. (a) Vertical slice along 16°N; (b) Vertical slice along 12°N; (c) Vertical slice along 8°N; (d) Vertical slice along 4°N; (e) Vertical slice along 0°N. Red color and blue color represent low and high velocity anomalies, respectively. The two dashed lines in the slices indicate the 410 and 660 km discontinuities, respectively. The velocity anomaly scale is shown at the bottom.

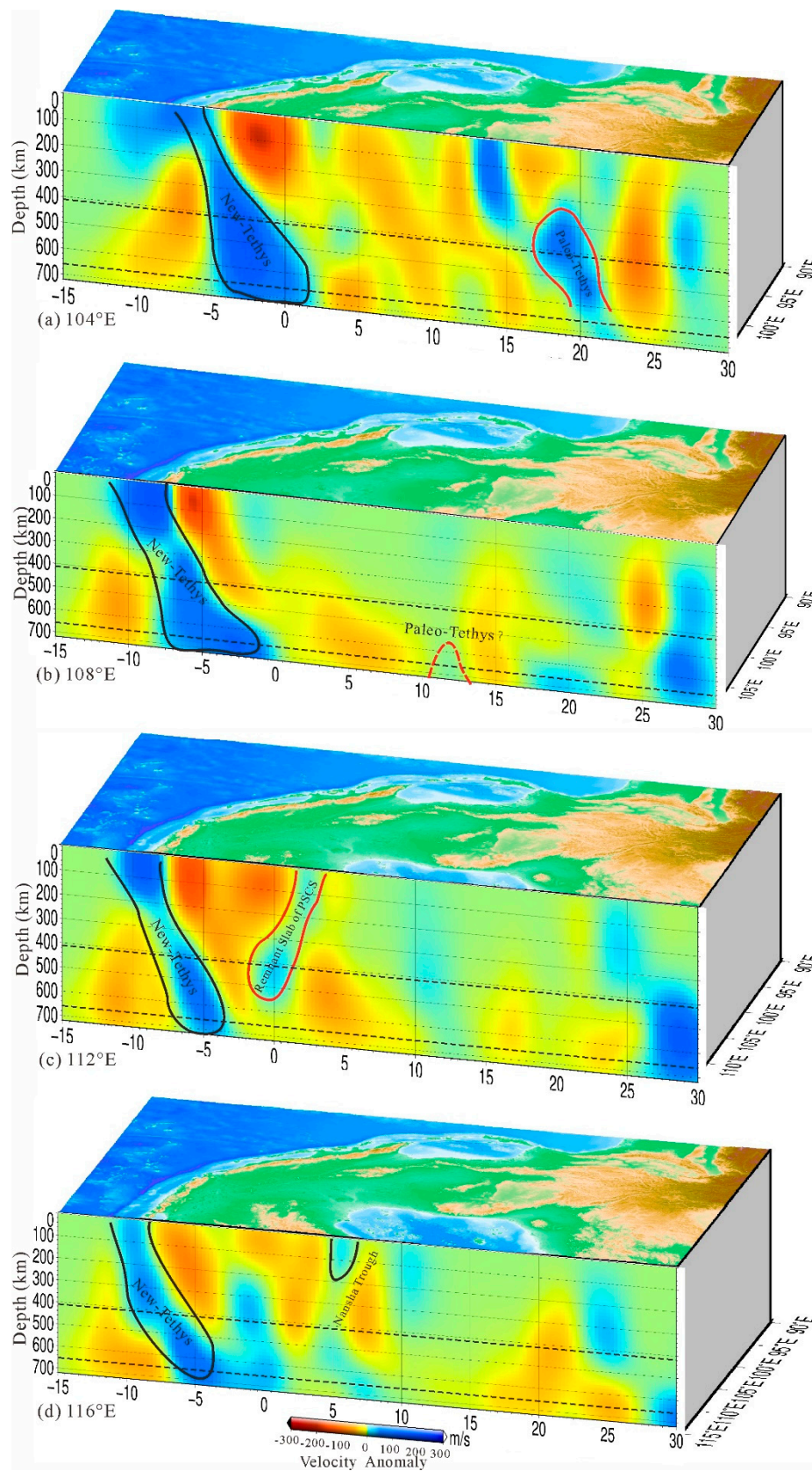


Figure 13. Four vertical slices of the P-wave velocity tomography along the longitude direction. (a) Vertical slice along 104°E; (b) Vertical slice along 108°E; (c) Vertical slice along 112°E; (d) Vertical slice along 116°E. Red color and blue color represent low and high velocity anomalies, respectively. The two dashed lines in the slices indicate the 410 and 660 km discontinuities, respectively. The velocity anomaly scale is shown at the bottom.

We then compared our 3D P-wave velocity model in the study area with previous studies on seismic tomography imaging conducted in the same region [73–77] or on a global scale [78–81]. Our results were basically consistent with the previous results: high-velocity anomalies were located below the plate boundary and island arcs such as the southeastern Tibet Plateau, South China Plate, the Philippines, Sumatra, and Java and low-velocity anomalies were located in the deep part of the SCS basin and the shallow part of Borneo. What is worth noting in the results of this study is the high-velocity anomaly discovered on the Indochina–Natuna Island–Borneo–Palawan, which may indicate the location of the sutures of the PSCS, which will be discussed in detail in the next section.

7. Discussion

The three-dimensional velocity model obtained in this paper can provide more evidence for studying the tectonic evolution of the PSCS. According to previous studies on the PSCS, some scholars believed that the stitching position of PSCS was in central Borneo [8,82]. Some authors have found that the magnetic anomaly of the satellite shows that the lower part of Natuna Island exhibited the same low magnetic anomaly as the ocean basin area, and then inferred that it may be the location of the PSCS suture in the area [83]. While agreeing with the above conclusion, this paper argues that the PSCS suture should extend northeastward to Palawan, and extend northwestward to Indochina. The ophiolites on the Lupar line in the southern SCS are distributed along the line from Natuna Island–Northern Borneo–Southern Palawan [84,85]. Ophiolite, as a representative of ancient lithosphere fragments, indicates that the above path may be a suture zone of the PSCS. According to the characteristics of the velocity anomalies at different depths, during the demise of the PSCS, some plates may remain in the mantle, which provides guidance for us to restore the position of the PSCS (Figure 10).

According to the position of the PSCS sutures delineated in the horizontal slices, the velocity anomalies on the east–west slices through the sutures were analyzed. In the slice along 16°N (Figure 12a), a high-velocity body was located in the area of 96°E–106°E and a depth range of 240 km–660 km (red solid area in Figure 12a). The high-velocity body was covered by the low velocity body, which was also revealed in a previous tomographic model [31,86]. We inferred the high-velocity body to a remnant slab of Paleo-Tethys. In the slice along 12°N, in the area of 104°–106°, in the depth range of 500 km–720 km, a similar high-velocity body was also found (red solid area in Figure 12b), where we inferred that the high-velocity body was also the remnant slab of Paleo-Tethys. In the 8°N slice, only a small area of high-velocity body was located below 600 km near 105° (Figure 12c red dotted area), where the high-velocity body may also be the remains of Paleo-Tethys. The smaller scale may be caused by the upwelling and melting of the hot material caused by the subduction of the plate. Coincidentally, in the slice along 4°N, a high-velocity body subduction eastward was found within the range of 108°E–117°E (red solid area in Figure 12d), and the deepest point reached below 660 km. The low-velocity anomalies above Borneo were caused by the upwelling of the material due to the subduction of the plate into the mantle. A high-velocity body subduction eastward was also found along the 0°N slice, in the range 106°E–116°E (Figure 12e), with a low-velocity anomaly caused by the upwelling of the mantle material above it. Some scholars concluded that the PSCS subducted mainly southward beneath Borneo during 45 Ma and 16 Ma [6,87]. Previous researchers have also found a high-velocity anomaly dipping S–SE below northern Borneo [30,88]. Therefore, we infer that the high-velocity body is a remnant slab of the PSCS subducting below Borneo. However, we believe that the slab-pull of the PSCS was not the main factor for the opening of the SCS. A high-velocity body subduction eastward (black solid area in Figure 12) was located on the westernmost side of the east–west slice. According to its position distribution, it should indicate the subduction zone of New-Tethys. It is worth noting that on the 4°N section, another high-velocity body (yellow solid area in Figure 12d) was located on the west side of the high-velocity belt representing the subduction of New-Tethys, and it is speculated that this high-velocity body may be the subduction of Mid-Tethys. Based on the above results, we have revised the positions of Mid-Tethys and Paleo-Tethys proposed by our predecessors (Figure 15).

Similarly, based on the location of the PSCS suture delineated in the horizontal slices, the velocity on the north–south slice passed through the suture location anomalies for analysis. In the slice along 104°E (Figure 13a), a high-velocity body was located within the depth range of 240 km–660 km in the area of 15°N – 20°N (red solid area in Figure 13a). This high-velocity body coincides with the position of the high-velocity body found in Figure 12a. It can be inferred that the high-velocity body is a remnant plate of Paleo-Tethys, and the high-velocity body is covered by the low velocity body. This phenomenon has been revealed by previous study [31,86]. In the slice along 108°E , due to less rays in this region only in the range 10°N – 13°N , the high-velocity bodies with suspected Paleo-Tethys remnant slabs were located below 600 km (the area circled by the red dashed line in Figure 13b). On the 112°E slice, in the range of 4°N – 2°S , a high-velocity body was found diving southward to below Borneo (Figure 13c red dashed line circled the area) up to 600 km deep, and the high-velocity body was presumed to be a remnant plate of the PSCS. On the slice along 116°E , within the range of 7°N – 4°N , a high-velocity body subduction southward (Figure 13d black solid line circled the area) was found within the range, and the deepest point reached below 220 km. Some scholars believed that the slab-pull of the PSCS will cause the southward movement of the Dangerous Grounds and the thinning of the crust [89]. Therefore, we speculate that the high-velocity body is a remnant plate subduction from the Nansha Trough below Borneo. Based on the velocity anomaly signature, we inferred that the Nansha Trough and the Dangerous Grounds were the same tectonic unit. The northward high-velocity body was located at the southernmost end of the north–south slices, and it can be inferred that this high-velocity zone indicated the New-Tethys subduction. It is worth noting that the shallower Borneo exhibited low velocity anomalies that were caused by material upwelling due to the penetration of the Mid-Tethys and the PSCS to the mantle (Figure 14).

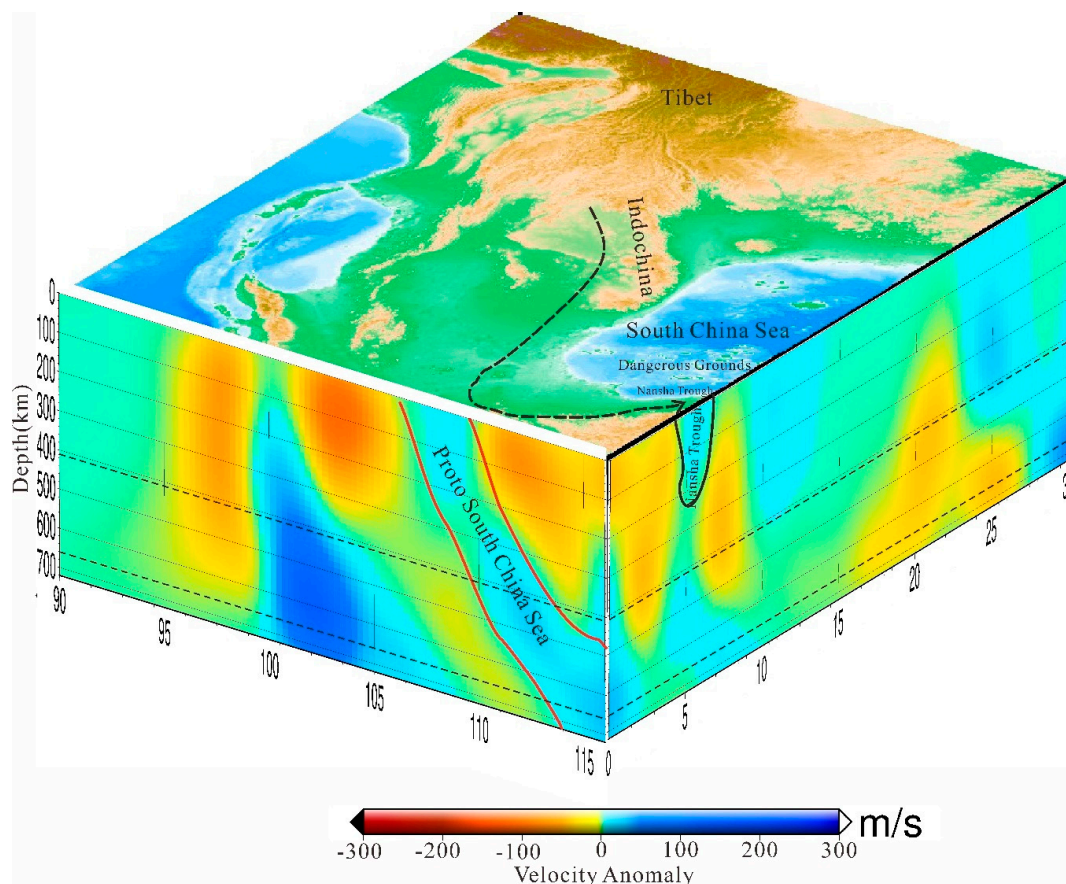


Figure 14. Cartoon diagram denotes the suture location of the PSCS.

Based on the above viewpoint, combined with the velocity anomalies characteristic of the Indochina–Natuna Island–Borneo–Palawan, we concluded that the PSCS from Indochina is in a nearly north–south direction, passing northeast of Natuna Island to western Borneo and turning to a nearly east–west direction. It finally turned north–eastward in northern Borneo, reaching Palawan and connecting with the suture belt of the Paleo-Pacific Ocean. The exact path is shown by the solid line with red arrows in Figure 11.

In summary, our results suggest that the PSCS is both the southern branch of Paleo-Tethys and a channel between Paleo-Tethys and the Paleo-Pacific Ocean. The location of the PSCS suture should be distributed along the Indochina–Natuna Island–Borneo–Palawan. The specific route is shown in the solid black line with arrows in Figures 14 and 15. We speculate that the northeast end of the PSCS is connected with the subduction zone of the Paleo-Pacific near Palawan Island. Due to the northward backlog of the Australian plate, the PSCS finally closed from west to east in a scissor-like fashion, and died out under Borneo. As shown in Figure 15, the blue dotted line indicates the location of the sutures of Paleo-Tethys–PSCS–Paleo-Pacific.

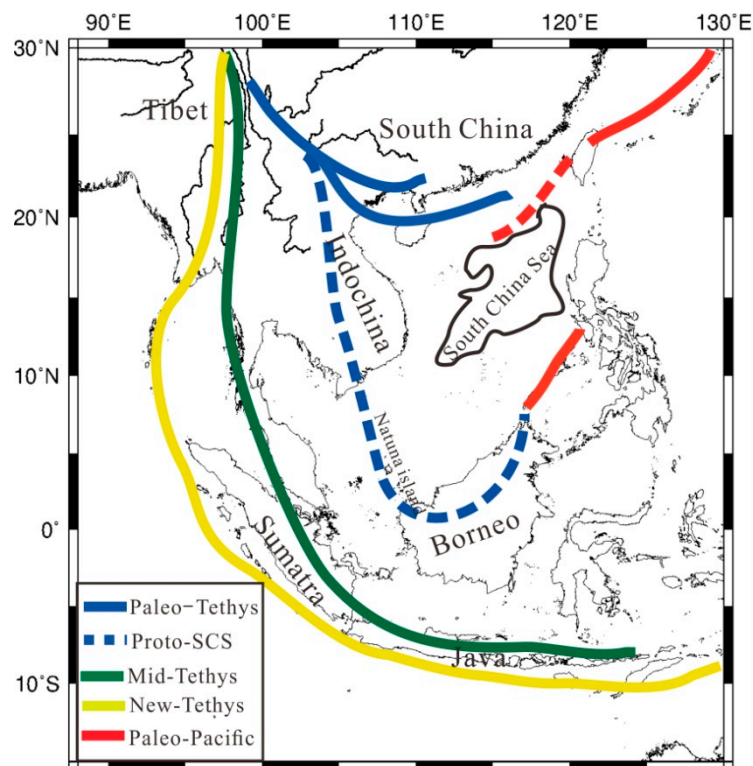


Figure 15. Schematic diagram of the spread of the PSCS with Tethys and the ancient Pacific in Southeast Asia (modified from Zhou et al. [8]).

8. Conclusions

We presented here a three-dimensional P-wave velocity beneath SE Asia using extensive relative travel time residual data obtained from ISC (International Seismic Center) [34] and IRIS (Incorporated Research Institutions for Seismology) [33]. Although the stations are mainly located in regions such as land and island arcs, the abundance of seismic events ensured the reliability of the results of this study.

Our results revealed the velocity structure of the upper mantle beneath the SE Asia. It was found that high-velocity anomalies were mainly located in regions such as the southeastern Tibetan Plateau, the Philippines, Sumatra, Java, and deep Borneo, and low velocity anomalies were mainly located in the deep parts of the SCS basin and in the shallower areas near the subduction zone such as Borneo. High-velocity anomalies mainly suggest subduction plates and stable continental blocks, while low-velocity anomalies suggest island arcs and upwelling of mantle material caused by subduction plates.

We found a southward subducting high-velocity body in the Nansha Trough, which is presumed to be a remnant of the subduction of the Dangerous Grounds into Borneo. We further inferred that the Nansha Trough and the Dangerous Grounds belong to the same tectonic unit.

A high-velocity body was located in the deep beneath the Indochina–Natuna Island–Borneo–Palawan. The location of the high-velocity body is consistent with the distribution range of the ophiolite belt, so it is speculated that the high-velocity body indicating the PSCS and the Paleo-Tethys. Residue. PSCS was the southern branch of Mid-Tethys, and it was also the channel connecting Paleo-Tethys and the Paleo-Pacific Ocean. Due to the squeeze of the Australian plate, PSCS closed from west to east in a scissor-style, and eventually died out under Borneo. We believe that the slab-pull of the PSCS was not the controlling factor for the opening of the SCS.

Author Contributions: Conceptualization, T.L. and G.Z.; Methodology, R.Z. and H.S.; Software, H.S.; Validation, R.Z. and T.L.; Formal analysis, H.S. and H.Y.; Investigation, H.S.; Resources, G.Z.; Data curation, H.Y.; Writing—original draft preparation, H.S.; Writing—review and editing, T.L., H.S., and R.Z.; Visualization, H.S.; Supervision, R.Z.; Project administration, G.Z. and T.L.; Funding acquisition, G.Z. All authors have read and agreed to the published version of the manuscript.

Funding: This research was funded by the National Major Science and Technology Projects of China: Key technology of oil and gas exploration in deep water area of the South China Sea under Grant 2016ZX05026-007-001, and the China Postdoctoral Science Foundation under Grant 2020TQ0114.

Acknowledgments: The natural seismic tomography study in this paper was based on Rawlinson’s program and was gratefully acknowledged, as are the seismic data provided by IRIS and ISC, and the mapping of the relevant maps in this paper was carried out using GMT software, with thanks to Wessel and Smith [90], the authors of this software.

Conflicts of Interest: The authors declare no conflict of interest.

References

1. Liu, H.; Xie, G.; Yan, P.; Liu, Y.; Zheng, H. Tectonic implication of Mesozoic marine deposits in the Nansha islands of the South China Sea. *Oceanol. Limnol. Sin.* **2007**, *38*, 272–278.
2. Zhou, D.; Wu, S.; Chen, H. The dynamics of tectonic evolution in the Nansha sea area and adjacent areas. *Earth Tecton. Mineral.* **2005**, *29*, 339–345.
3. Taylor, B.; Hayes, D.E. *Origin, and History of the South China Sea Basin*; John Wiley & Sons, Inc.: Hoboken, NJ, USA, 1983; pp. 23–56. [[CrossRef](#)]
4. Holloway, N.H. North Palawan block, Philippines—Its relation to Asian mainland and role in evolution of south china sea. *Bull. Am. Assoc. Petrol. Geol.* **1982**, *66*, 1355–1383. [[CrossRef](#)]
5. Hall, R. Contraction, and extension in northern Borneo driven by subduction rollback. *J. Asian Earth Sci.* **2013**, *76*, 399–411. [[CrossRef](#)]
6. Hall, R.; van Hattum, M.W.A.; Spakman, W. Impact of India—Asia collision on SE Asia: The record in Borneo. *Tectonophysics* **2008**, *451*, 366–389. [[CrossRef](#)]
7. Zahirovic, S.; Matthews, K.J.; Flament, N.; Müller, R.D.; Hill, K.C.; Seton, M.; Gurnwas, M. Tectonic evolution and deep mantle structure of the eastern Tethys since the latest Jurassic. *Earth Sci. Rev.* **2016**, *162*, 293–337. [[CrossRef](#)]
8. Zhou, D.; Sun, Z. Plate evolution in the Pacific domain since Late Mesozoic and its inspiration to tectonic research of East Asia margin. *J. Trop. Oceanogr.* **2017**, *36*, 1–19.
9. Fan, J.; Zhao, D.; Dong, D.; Zhang, G. P-wave tomography of subduction zones around the central Philippines and its geodynamic implications. *J. Asian Earth Sci.* **2017**, *146*, 76–89. [[CrossRef](#)]
10. Wu, J.; Suppe, J. Proto-SCS Plate Tectonics Using Subducted Slab Constraints from Tomography. *J. Earth Sci.* **2017**, *29*, 1304–1318. [[CrossRef](#)]
11. Wu, J.; Suppe, J.; Lu, R.; Kanda, R. Philippine Sea and East Asian plate tectonics since 52 Ma constrained by new subducted slab reconstruction methods. *J. Geophys. Res. Solid Earth* **2016**, *121*, 4670–4741. [[CrossRef](#)]
12. Wu, S.; Zhou, D.; Liu, H. Tectonic framework and evolutionary characteristics of Nansha Block, South China Sea. *Geotecton. Metallog.* **2004**, *28*, 23–28.
13. Zhou, D.; Sun, Z.; Chen, H. Mesozoic lithofacies, paleo-geography, and tectonic evolution of the South China Sea and surrounding areas. *Earth Sci. Front.* **2005**, *12*, 204–218.

14. Metcalfe, I. Tectonic framework, and Phanerozoic evolution of Sundaland. *Gondwana Res.* **2011**, *19*, 3–21. [[CrossRef](#)]
15. Lu, B.; Wang, P.; Liang, J.; Zhou, D.; Sun, Z.; Chen, H.Z.; Xu, H.H.; Wang, W.Y.; Pang, X.; Cai, D.S.; et al. Tectonic properties of the Proto-SCS and their relationship with the Tethys and Paleo-Pacific tectonic domains. *J. Jilin Univ. Earth Sci. Ed.* **2014**, *4*, 1441–1450.
16. Müller, R.D.; Seton, M.; Zahirovic, S.; Williams, S.E.; Matthews, K.J.; Wright, N.M.; Shephard, G.E.; Maloney, K.T.; Barnett-Moore, N.; Hosseinpour, M.; et al. Ocean Basin Evolution and Global-Scale Plate Reorganization Events Since Pangea Breakup. *Annu. Rev. Earth Planet. Sci.* **2016**, *44*, 107–138. [[CrossRef](#)]
17. Chen, Z. Tethyan geology for 100 years. *Tethyan Geol.* **1994**, *18*, 1–22. (In Chinese)
18. Pan, G. An Evolution of tethys in global ocean continent transformation. *Tethyan Geol.* **1994**, *18*, 23–40. (In Chinese)
19. Metcalfe, I. Gondwanaland dispersion, Asian accretion, and evolution of eastern Tethys. *Aust. J. Earth Sci.* **1996**, *43*, 605–623. [[CrossRef](#)]
20. Metcalfe, I. Gondwana dispersion and Asian accretion: Tectonic and palaeogeographic evolution of eastern Tethys. *J. Asian Earth Sci.* **2013**, *66*, 1–33. [[CrossRef](#)]
21. Hongfu, Y.; Shunbao, W.; Yuansheng, D.; Yuanqiao, P. South China defined as part of tethyan archipelagic ocean system. *Earth Sci. J. China Univ. Geosci.* **1999**, *24*, 1–12. (In Chinese)
22. Engebretson, D.C.; Cox, A.; Gordon, R.G. Relative motions between oceanic and continental plates in the Pacific basin. *Geol. Soc. Am. Spec. Pap.* **1985**, *206*, 1–60.
23. Wessel, P.; Kroenke, L.W. Pacific absolute plate motion since 145 Ma: An assessment of the fixed hot spot hypothesis. *J. Geophys. Res.* **2008**, *113*. [[CrossRef](#)]
24. Müller, R.D.; Sdrolias, M.; Gaina, C.; Roest, W.R. Age, spreading rates, and spreading asymmetry of the world's ocean crust. *Geochem. Geophys. Geosystems* **2008**, *9*, Q04006. [[CrossRef](#)]
25. Seton, M.; Müller, R.D.; Zahirovic, S.; Gaina, C.; Torsvik, T.; Shephard, G.; Talsma, A.; Gurnis, M.; Turner, M.; Maus, S.; et al. Global continental and ocean basin reconstructions since 200 Ma. *Earth Sci. Rev.* **2012**, *113*, 212–270. [[CrossRef](#)]
26. Wright, N.M.; Seton, M.; Williams, S.E.; Müller, R.D. The Late Cretaceous to recent tectonic history of the Pacific Ocean basin. *Earth Sci. Rev.* **2016**, *154*, 138–173. [[CrossRef](#)]
27. Rawlinson, N.; Pozgay, S.; Fishwick, S. Seismic tomography: A window into deep Earth. *Phys. Earth Planet. Inter.* **2010**, *178*, 101–135. [[CrossRef](#)]
28. Cao, X.-L.; Zhu, J.-S.; Zhao, L.-F.; Cao, J.-M.; Hong, X.-h. Three-dimensional shear wave velocity structure of crust and upper mantle in SCS and its adjacent regions by surface waveform inversion. *Acta Seismol. Sin.* **2001**, *23*, 113–124.
29. Huang, Z.X.; XU, Y. S-velocity structure of SCS and surrounding regions from surface wave tomography. *Chin. J. Geophys.* **2011**, *54*, 3089–3097.
30. Tang, Q.; Zheng, C. Crust and upper mantle structure and its tectonic implication in the SCS and adjacent regions. *J. Asian Earth Sci.* **2013**, *62*, 510–525. [[CrossRef](#)]
31. Huang, Z.; Zhao, D.; Wang, L. P wave tomography and anisotropy beneath Southeast Asia: Insight into mantle dynamics. *J. Geophys. Res. Solid Earth* **2015**, *120*, 5154–5174. [[CrossRef](#)]
32. JianZhong, Z.; ZhiWei, L.; JianMin, L.; TianYao, H.; Feng, B.; Jun, X.; LiaoLiang, W.; GuangHong, T. Ambient noise tomography and deep structure in the crust and mantle of the South China Sea. *Chin. J. Geophys* **2019**, *62*, 2070–2087. (In Chinese) [[CrossRef](#)]
33. IRIS DMC. Data Access Tutorial for the IRIS Data Management Center, IRIS Data Management System. 1994. Available online: <https://ds.iris.edu/ds/nodes/dmc/> (accessed on 31 July 2020).
34. Engdahl, E.R.; Di Giacomo, D.; Sakarya, B.; Gkarlaouni, C.G.; Harris, J.; Storchak, D.A. ISC-EHB 1964-2016, an Improved Data Set for Studies of Earth Structure and Global Seismicity. *Earth Space Sci.* **2020**, *7*, e2019EA000897. [[CrossRef](#)]
35. Li, X.; Hao, T.; Li, Z. Upper mantle structure and geodynamics of the Sumatra subduction zone from 3-D teleseismic P-wave tomography. *J. Asian Earth Sci.* **2018**, *161*, 25–34. [[CrossRef](#)]
36. Vandecar, J.C.; Crosson, R.S. Determination of teleseismic arrival times using multi-channel cross-correlation and least squares. *Bull. Seismol. Soc. Am.* **1990**, *80*, 150–169.

37. Rawlinson, N.; Kennett, B.L.; Reading, A.M. 3-D Teleseismic Tomography of the Crust and Upper Mantle Beneath Northern Tasmania, Australia. In Proceedings of the AGU Fall Meeting, San Francisco, CA, USA, 13–17 December 2004.
38. Jiang, G.-M.; Zhang, G.B.; Xu, X. Fast method, and application of teleseismic relative time-travel data. *J. Geophys.* **2012**, *12*, 221–229.
39. Jia, Z.; Zhang, G. Teleseismic Tomography for Imaging the Upper Mantle Beneath Northeast China. *Appl. Sci.* **2020**, *10*, 4557. [[CrossRef](#)]
40. Rawlinson, N.; Kennett, B.L.N. Rapid estimation of relative and absolute delay times across a network by adaptive stacking. *Geophys. J. R. Astron. Soc.* **2004**, *157*, 332–340. [[CrossRef](#)]
41. Zhang, F.X.; Wu, Q.J.; Li, Y.H. The traveltimes tomography study by Teleseismic P wave data in the Northeast area. *Chin. J. Geophys.* **2013**, *56*, 2690–2700. (In Chinese)
42. Benz, H.M.; Zandt, G.; Oppenheimer, D.H. Lithospheric structure of northern California from teleseismic images of the upper mantle. *J. Geophys. Res.* **1992**, *97*, 4791–4807. [[CrossRef](#)]
43. Saltzer, R.L.; Humphreys, E.D. Upper mantle P wave velocity structure of the eastern Snake River Plain and its relationship to geodynamic models of the region. *J. Geophys. Res.* **1997**, *102*, 11829–11841. [[CrossRef](#)]
44. Frederiksen, A.W.; Bostock, M.G.; Van Decar, J.C.; Cassidy, J.F. Seismic structure of the upper mantle beneath the northern Canadian Cordillera from teleseismic travel-time inversion. *Tectonophysics* **1998**, *294*, 43–55. [[CrossRef](#)]
45. Rawlinson, N.; Sambridge, M. The fast marching method: An effective tool for tomographic imaging and tracking multiple phases in complex layered media. *Explor. Geophys.* **2005**, *36*, 341–350. [[CrossRef](#)]
46. Thomson, C.J.; Gubbins, D. Three-dimensional lithospheric modelling at NORSAR: Linearity of the method and amplitude variations from the anomalies. *Geophys. J. R. Astr. Soc.* **1982**, *71*, 1–36. [[CrossRef](#)]
47. Rawlinson, N.; De Kool, M.; Sambridge, M. Seismic wavefront tracking in 3D heterogeneous media: Applications with multiple data classes. *Explor. Geophys.* **2006**, *37*, 322–330. [[CrossRef](#)]
48. Sethian, J.A.; Popovici, A.M. 3-D traveltimes computation using the fast marching method. *Geophysics* **1999**, *64*, 516–523. [[CrossRef](#)]
49. Popovici, A.M.; Sethian, J.A. 3-D imaging using higher order fast marching traveltimes. *Geophysics* **2002**, *67*, 604–609. [[CrossRef](#)]
50. Tarantola, A. *Inverse Problem Theory*; Elsevier: Amsterdam, The Netherlands, 1987.
51. Kennett, B.L.N.; Sambridge, M.S.; Williamson, P.R. Subspace methods for large scale inverse problems involving multiple parameter classes. *Geophys. J.* **1988**, *94*, 237–247. [[CrossRef](#)]
52. Sambridge, M.S. Non-linear arrival time inversion: Constraining velocity anomalies by seeking smooth models in 3-D. *Geophys. J. Int.* **1990**, *102*, 653–677. [[CrossRef](#)]
53. Williamson, P.R. Tomographic inversion in reflection seismology. *Geophys. J. Int.* **1990**, *100*, 255–274. [[CrossRef](#)]
54. Blundell, C.A. Resolution Analysis of Seismic P-Wave Velocity Estimates Using Reflection Tomographic Inversion. Ph.D. Thesis, Monash University, Victoria, Australia, 1993.
55. Wang, Y.; Houseman, G.A. Inversion of reflection seismic amplitude data for interface geometry. *Geophys. J. Int.* **1994**, *117*, 92–110. [[CrossRef](#)]
56. Wang, Y.; Houseman, G.A. Tomographic inversion of reflection seismic amplitude data for velocity variation. *Geophys. J. Int.* **1995**, *123*, 355–372. [[CrossRef](#)]
57. Rawlinson, N.; Reading, A.M.; Kennett, B.L.N. Lithospheric structure of Tasmania from a novel form of teleseismic tomography. *J. Geophys. Res.* **2006**, *111*.
58. Rawlinson, N.; Kennett, B.L.N.; Heintz, M. Insights into the structure of the upper mantle beneath the Murray basin from 3D teleseismic tomography. *Aust. J. Earth Sci.* **2006**, *53*, 595–604. [[CrossRef](#)]
59. Rawlinson, N.; Houseman, G.A.; Collins, C.D.N. Inversion of seismic refraction and wide-angle reflection traveltimes for 3-D layer crustal structure. *Geophys. J. Int.* **2001**, *145*, 381–401. [[CrossRef](#)]
60. Li, Z.W.; Ni, S.D.; Hao, T.Y.; Xu, Y.; Roecker, S. Uppermost mantle structure of the eastern margin of the Tibetan plateau from interstation Pn traveltimes difference tomography. *Earth Planet. Sci. Lett.* **2012**, *335–336*, 195–205. [[CrossRef](#)]
61. Li, Z.W.; Tian, B.F.; Liu, S.; Yang, J.S. Asperity of the 2013 Lushan earthquake in the eastern margin of Tibetan plateau from seismic tomography and aftershock relocation. *Geophys. J. Int.* **2013**, *195*, 2016–2022. [[CrossRef](#)]

62. Li, Z.W.; Roecker, S.; Kim, K.H.; Xu, Y.; Hao, T.Y. Moho depth variations in the Taiwan orogen from joint inversion of seismic arrival time and Bouguer gravity data. *Tectonophysics* **2014**, *632*, 151–159. [[CrossRef](#)]
63. Li, Z.W.; Ni, S.D.; Zhang, B.L.; Bao, F.; Zhang, S.Q.; Deng, Y.; Yuen, D. Shallow magma chamber under the Wudalianchi Volcanic Field unveiled by seismic imaging with dense array. *Geophys. Res. Lett.* **2016**, *43*, 4954–4961. [[CrossRef](#)]
64. Zietlow, D.W.; Molnar, P.H.; Sheehan, A.F. Teleseismic P-wave tomography of South Island, New Zealand upper mantle: Evidence of subduction of Pacific lithosphere since 45 Ma. *J. Geophys. Res.* **2016**, *121*, 4427–4445. [[CrossRef](#)]
65. Tian, Y.; Huang, S.H.; Nolet, G.; Montelli, R.; Dahlen, F.A. Dynamic ray tracing and traveltimes corrections for global seismic tomography. *J. Comput. Phys.* **2007**, *226*, 672–687. [[CrossRef](#)]
66. Obayashi, M.; Suetsugu, D.; Fukao, Y. PP-P differential traveltimes measurement with crustal correction. *Geophys. J. Int.* **2004**, *157*, 1152–1162. [[CrossRef](#)]
67. Jiang, G.-M.; Zhao, D.P.; Zhang, G.B. Crustal correction in teleseismic tomography and its application. *Chin. J. Geophys.* **2009**, *52*, 1508–1514.
68. Kennett, B.L.N.; Engdahl, E.R.; Buland, R. Constraints on seismic velocities in the Earth from traveltimes. *Geophys. J. Int.* **1995**, *122*, 108–124. [[CrossRef](#)]
69. Laske, G.; Masters, G.; Ma, Z.; Pasyanos, M. Update on CRUST1.0—A 1-degree global model of Earth’s crust. In Proceedings of the EGU General Assembly Conference, Vienna, Austria, 7–12 April 2013; Volume 15, p. 2658.
70. Rawlinson, N.; Sambridge, M. Seismic traveltimes tomography of the crust and lithosphere. *Adv. Geophys.* **2003**, *46*, 81–198.
71. Zhao, D.; Yanada, T.; Hasegawa, A.; Umino, N.; Wei, W. Imaging the subducting slabs and mantle upwelling under the Japan islands. *Geophys. J. Int.* **2012**, *190*, 816–828. [[CrossRef](#)]
72. Zhao, D.; Yu, S.; Liu, X. Seismic anisotropy tomography: New insight into subduction dynamics. *Gondwana Res.* **2015**. [[CrossRef](#)]
73. Bijwaard, H.; Spakman, W.; Engdahl, E.R. Closing the gap between regional and global travel time tomography. *J. Geophys. Res.* **1998**, *103*, 30055–30078. [[CrossRef](#)]
74. Fukao, Y.; Obayashi, M. Subducted slabs stagnant above, penetrating through, and trapped below the 660 km discontinuity. *J. Geophys. Res. Solid Earth* **2013**, *118*, 5920–5938. [[CrossRef](#)]
75. Li, C.; van der Hilst, R.D.; Engdahl, E.R.; Burdick, S. A new global model for P wave speed variations in Earth’s mantle. *Geochem. Geophys. Geosyst.* **2008**, *9*, Q05018. [[CrossRef](#)]
76. Simmons, N.A.; Myers, S.C.; Johannesson, G.; Matzel, E. LLNL-G3Dv3: Global P wave tomography model for improved regional and teleseismic travel time prediction. *J. Geophys. Res.* **2012**, *117*, B10302. [[CrossRef](#)]
77. Zhao, D.; Yamamoto, Y.; Yanada, T. Global mantle heterogeneity and its influence on teleseismic regional tomography. *Gondwana Res.* **2013**, *23*, 595–616. [[CrossRef](#)]
78. Huang, J.; Zhao, D. High-resolution mantle tomography of China and surrounding regions. *J. Geophys. Res.* **2006**, *111*, B09305. [[CrossRef](#)]
79. Huang, Z.; Wang, P.; Zhao, D.; Wang, L.; Xu, M. Three-dimensional P wave azimuthal anisotropy in the lithosphere beneath China. *J. Geophys. Res. Solid Earth* **2014**, *119*, 5686–5712. [[CrossRef](#)]
80. Pesicek, J.D.; Thurber, C.H.; Widiyantoro, S.; Zhang, H.; DeShon, H.R.; Engdahl, E.R. Sharpening the tomographic image of the subducting slab below Sumatra, the Andaman island and Burma. *Geophys. J. Int.* **2010**, *182*, 433–453. [[CrossRef](#)]
81. Wei, W.; Xu, J.; Zhao, D.; Shi, Y. East Asia mantle tomography: New insight into plate subduction and intraplate volcanism. *J. Asian Earth Sci.* **2012**, *60*, 88–103. [[CrossRef](#)]
82. Zhou, D.; Sun, Z.; Chen, H.; Xu, H. Mesozoic paleogeography and tectonic evolution of SCS and adjacent areas in the context of Tethyan and Paleo-Pacific interconnections. *Isl. Arc* **2008**, *17*, 186–207. [[CrossRef](#)]
83. Li, T.L.; Shi, H.Y.; Guo, Z.H.; Zhang, G.; Zhang, R.; Chen, H. Research on deep structure of the SCS based on satellite gravity and magnetic data. *Chin. J. Geophys.* **2018**, *61*, 334–348. (In Chinese)
84. Yumul, G.P., Jr.; Dimalanta, C.B.; Marquez, E.J.; Queaño, K.L. Onland signatures of the Palawan micro-continental block and Philippine mobile belt collision and crustal growth process: A review. *J. Asian Earth Sci.* **2009**, *34*, 610–623. [[CrossRef](#)]
85. Hutchison, C.S. *Geology of North-West Borneo: Barawak, Brunei and Babah*; Elsevier: Amsterdam, The Netherlands, 2005; Volume 444.

86. Widiyantoro, S.; van der Hilst, R. Structure and evolution of lithospheric slab beneath the Sunda Arc, Indonesia. *Science* **1996**, *271*, 1566–1570. [[CrossRef](#)]
87. Clift, P.; Lee, G.H.; Duc, N.A.; Barckhausen, U.; Van Long, H.; Zhen, S. Seismic reflection evidence for a dangerous ground's miniplate: No extrusion origin for the South China Sea. *Tectonics* **2008**, *27*, TC3008. [[CrossRef](#)]
88. Rangin, C.; Spakman, W.; Pubellier, M.; Bijwaard, H. Tomographic and geological constraints on subduction along the eastern Sundaland continental margin (South-East Asia). *Bull. Soc. Geol. Fr.* **1999**, *170*, 775–788.
89. Cullen, A.; Reemst, P.; Henstra, G.; Gozzard, S.; Ray, A. Rifting of the South China Sea: New perspectives. *Petrol. Geosci.* **2010**, *16*, 273–282. [[CrossRef](#)]
90. Wessel, P.; Smith, W.H. New, Improved version of the generic mapping tools released. *Eos Trans. AGU* **1998**, *79*, 579. [[CrossRef](#)]



© 2020 by the authors. Licensee MDPI, Basel, Switzerland. This article is an open access article distributed under the terms and conditions of the Creative Commons Attribution (CC BY) license (<http://creativecommons.org/licenses/by/4.0/>).